Water-exchange MRI detects subtle blood-brain barrier breakdown in Alzheimer's disease rats

DOI:
10.1016/j.neuroimage.2018.09.030

Document Version
Accepted author manuscript

Accepted Manuscript

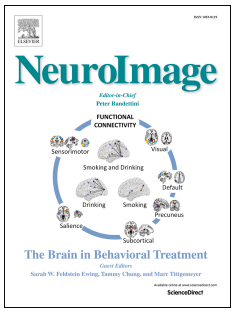

Water-exchange MRI detects subtle blood-brain barrier breakdown in Alzheimer's disease rats

Ben R. Dickie, Matthias Vandesquille, José Ulloa, Hervé Boutin, Laura M. Parkes, Geoff.J.M. Parker

PII: S1053-8119(18)30815-2

DOI: 10.1016/j.neuroimage.2018.09.030

Reference: YNIMG 15266

To appear in: *NeuroImage*

Received Date: 24 May 2018

Revised Date: 5 September 2018

Accepted Date: 12 September 2018

Please cite this article as: Dickie, B.R., Vandesquille, M., Ulloa, José., Boutin, Hervé., Parkes, L.M., Parker, G.J.M., Water-exchange MRI detects subtle blood-brain barrier breakdown in Alzheimer's disease rats, *NeuroImage* (2018), doi: https://doi.org/10.1016/j.neuroimage.2018.09.030.

Title:

Water-exchange MRI detects subtle blood-brain barrier breakdown in Alzheimer's disease rats

Author names and affiliations:

Ben R. Dickie[1], Matthias Vandesquille[1], José Ulloa[2], Hervé Boutin[1], Laura M. Parkes[1,+], Geoff J. M. Parker[1,2,+]

1. Division of Neuroscience and Experimental Psychology, Faculty of Biology, Medicine, and Health, Stopford Building, University of Manchester, UK

2. Bioxydyn Ltd, Manchester, UK

[+]Joint senior authors

Corresponding author:
Ben.dickie@manchester.ac.uk

Present address:
Room G724a
Stopford Building
99 Oxford Road
The University of Manchester
M13 9PG

Abstract

Blood-brain barrier (BBB) breakdown has been hypothesized to play a key role in the onset and progression of Alzheimer's disease (AD). However, the question of whether AD itself contributes to loss of BBB integrity is still uncertain, as many *in-vivo* studies have failed to detect signs of AD-related BBB breakdown. We hypothesize AD-related BBB damage is subtle, and that these negative results arise from a lack of measurement sensitivity. With the aim of developing a more sensitive measure of BBB breakdown, we have designed a novel MRI scanning protocol to quantify the trans-BBB exchange of endogenous water. Using this method, we detect increased BBB water permeability in a rat model of AD that is associated with reduced expression of the tight junction protein occludin. BBB permeability to MRI contrast agent, assessed using dynamic contrast-enhanced (DCE)-MRI, did not differ between transgenic and wild-type animals and was uncorrelated with occludin expression. Our data supports the occurrence of AD-related BBB breakdown, and indicates that such BBB pathology is subtle and may be undetectable using existing 'tracer leakage' methods. Our validated water-exchange MRI method provides a new powerful tool with which to study BBB damage *in-vivo.*

Keywords: water-exchange, MRI, blood-brain barrier, Alzheimer's, permeability surface-area product, cerebrovascular dysfunction

1.1 Introduction

Loss of blood-brain barrier (BBB) integrity occurs in ageing (Farrall and Wardlaw, 2009; Montagne et al., 2016), and has been hypothesized to play a key role in the onset of Alzheimer's disease (AD) (Zlokovic, 2011). Growing evidence suggests BBB breakdown may occur when amyloid-β (Aβ) peptides interact with blood vessels in the brain, a process which causes arteriolar and capillary amyloid angiopathy (CAA) (Weller et al., 2008) and reduces the expression of BBB tight-junction proteins that maintain paracellular BBB integrity (Carrano et al., 2011; Keaney et al., 2015; Kook et al., 2012). Patients with AD typically have more severe CAA than age-matched non-AD patients (Vinters, 1987), which potentially exacerbates age-related cerebrovascular damage (Dorr et al., 2012) and alters Aβ clearance from the brain (Weller et al., 2008). However, the question of whether AD itself reduces BBB integrity remains unresolved, due to a number of conflicting studies (Bien-Ly et al., 2015; Caserta et al., 1998; Farrall and Wardlaw, 2009; Montagne et al., 2015; Schlageter et al., 1987; Starr et al., 2009; van de Haar et al., 2014; Wang et al., 1998)

Current methods for probing BBB integrity *in-vivo* monitor and detect the leakage of injectable small-molecular weight probes as they passively diffuse from blood to brain. However, in the case of an intact BBB or subtle BBB breakdown, leakage of these probes into tissue is slow, resulting in the need for long measurement durations to resolve differences in leakage between study groups (Armitage et al., 2011; Heye et al., 2016). Based on the known sensitivity of magnetic resonance imaging (MRI) to compartmental water exchange (Bains et al., 2010; Donahue et al., 1997; Landis et al., 1999), we have developed an MRI technique for detection of subtle BBB breakdown, based on measuring the trans-BBB transport of endogenous water. Specifically, we use an MRI contrast agent to shorten the spin-lattice relaxation time of blood, which increases the impact of trans-BBB water-exchange on MRI signals and makes possible the estimation of mean blood water residence time (τ_b) simultaneously with the blood water population fraction (p_b). The ratio of these measurements provides the trans-BBB permeability surface-area product to water (PS_w), a quantity we hypothesize to be more sensitive to subtle BBB breakdown compared to existing 'tracer leakage' measurements.

We first undertake sensitivity analyses and simulations to determine the optimal acquisition parameters for our water-exchange technique and to assess possible sources of bias in parameter estimates. The optimised MRI protocol, termed multi-flip angle multi-echo (MFAME)-MRI, is then used to measure BBB PS_w in a rat model of early-onset AD (TgF344-AD), alongside measures of contrast agent leakage rate, K^{trans}. Transgenic rats display increased PS_w relative to wild-type littermates, but BBB permeability to contrast agent remains unchanged. To understand the potential cause of increased PS_w, we then undertook immunostaining of tight junction proteins and show that PS_w correlates inversely with the expression of occludin at the BBB.

1.2 Material and methods

1.2.1 Sensitivity analysis

The change in spoiled gradient echo (SPGR) MRI signal, ΔS, due to unit changes in p_b, τ_b and PS_w was simulated using the SPGR-2S1X model (equations 3-6 to be found in section 1.2.5) for flip angles between 0-90 degrees, repetition times between 0-400 ms, and blood contrast agent concentrations (C_b) between 0-10 mM. A unit change was defined as a 50% increase in the parameter of interest. When varying flip angle, a TR = 100 ms and C_b = 4.8 mM was used. When varying TR, a flip angle = 30º and C_b = 4.8 mM was used. When varying C_b, a TR = 100 ms and a flip angle = 40º were used. A single set of representative tissue parameters were taken from the literature (Schwarzbauer et al., 1997; Zhang et al., 2013). Assuming 7T MRI these were: T_{1e} = 1.8 s, T_{1b} = 2.1 s, p_b = 0.020 mL mL^{-1}, Δp_b = 0.010 mL mL^{-1}, τ_b = 0.40 s, $\Delta\tau_b$ = 0.20 s and PS_w = 3.0 mL min^{-1} mL^{-1}, ΔPS_w = 1.5 mL min^{-1} mL^{-1}. Plots of $\Delta S/\Delta p_b$, $\Delta S/\Delta\tau_b$, and $\Delta S/\Delta PS_w$ versus flip angle, TR, and C_b were generated to determine the optimal acquisition parameters. Parameter definitions are given in section 1.2.5.

1.2.2 Monte Carlo Simulations

To estimate PS_w, the separate effects of p_b and τ_b on MRI signals must be distinguished. This requires acquisition of a minimum of 2 images with different flip angles or TRs, assuming all other model parameters are known. In this study we opt to acquire 5 flip angles while using a relatively long TR (100 ms). This protocol was chosen as opposed to using multiple TRs to provide an invariant and sufficient time delay between each RF pulse to acquire a multi-gradient echo readout for T_2* decay correction.

To determine the optimal use of imaging time, Monte Carlo simulations were performed to assess how the precision of p_b and τ_b estimates depend on the number of distinct post-contrast flip angles and image repetitions. Simulations were undertaken under the following conditions: 3 flip angles and 10 repeats (resulting in a total of 30 images), 4 flip angles and 7 or 8 repeats (also 30 images), and 5 flip angles and 6 repeats (also 30 images). For each simulation, flip angles were equally spaced across the range 10°- 80°. Each fit was repeated 100 times in a Monte Carlo simulation using a range of zero mean Gaussian noise levels (noise standard deviation/S_0 = 0.00001 to 0.004). Relative precision in parameter estimates was quantified using the coefficient of variation (CoV):

$$CoV = \frac{IQR(\hat{x})}{median(\hat{x})} \quad (1)$$

where IQR is the inter-quartile range, and $\hat{x}$ is the parameter estimate.

Next, we assessed the effect of transmit B_1 field (B_1^+) inhomogeneity and non-zero trans-BBB contrast agent leakage on SPGR-2S1X parameter estimates. Synthetic multiple-flip angle images (α = 10º, 20º, 40º, and 60º at a TR = 100 ms) were simulated for estimation of pre-contrast T_{1b} and T_{1t}. Dynamic SPGR images (α = 60°, TR = 20 ms) were generated to track $C_b(t)$ during a simulated injection of contrast agent. A population average $C_b(t)$ measured from the TgF344-AD rats was used. For estimation of p_b and τ_b, multiple flip angle images at 5 distinct flip angles (α = 10º, 20º, 30º, 40º, and 80º) were simulated. All images were created as 10 x 10 grids, giving 100 voxels in total.

To assess the effect of B_1^+ inhomogeneity on parameter estimates, images were generated across a range of realistic flip angle errors (±10%). Parameters p_b, τ_b, and pre-contrast T_{1e} and T_{1b}, were set to 0.02 mL mL^{-1}, 0.4 s, 1.8 s and 2.1 s, respectively (Schwarzbauer et al., 1997; Zhang et al., 2013). Contrast agent T_1 relaxivity (r_1) was assumed to be 3.5 $(mM\ s)^{-1}$ for both blood and tissue. Equation 1 was then fitted back to the simulated data assuming accurate flip angles. Relative bias of each parameter was estimated as:

$$\lambda = \frac{median(\hat{x}) - x}{x} \quad (2)$$

where $\hat{x}$ is the parameter estimate and x is the true parameter value (ground truth).

In an attempt to correct observed biases in parameter estimates due to B_1^+ inhomogeneity, an additional set of pre-contrast multi-flip angle images with a long TR were simulated (α = 5º, 10º, 20º, 30º, 40º, 60º, 80º, 90º, TR = 5000 ms). Varying the TR of SPGR images alters the T_1 and B_1^+ weighting (Voigt et al., 2010; Yarnykh, 2007). Thus, by jointly fitting SPGR signal models to long and short TR multi-flip angle images, we aim to remove the effects of B_1^+ inhomogeneity on estimates of T_1, and importantly PS_w. Simulations described above were repeated with the proposed flip angle correction method, and the bias in estimated parameters computed.

To simulate leakage of contrast agent across the BBB, T_{1e} was allowed to decrease in response to an increasing extravascular contrast agent concentration, $C_e(t)$. $C_e(t)$ was calculated from the two-compartment exchange model (Brix et al., 2004) using the population-based estimate of $C_b(t)$ and K^{trans} in the range 10^{-5} – 10^{-3} min^{-1}. Signal models (Eqn 3.) were then fit back to the simulated data assuming $K^{trans} = 0$ min^{-1}, and the bias in p_b, τ_b, and PS_w computed.

1.2.3 Animals

Male only TgF344-AD (n = 7) and wild-type (WT) littermates (n = 5) aged 18.3 months (range 17.9 - 18.8 months) were scanned using the MFAME-MRI protocol (see section 1.2.4 for details), then culled for immunohistochemistry. This rat model of AD has previously been shown to display widespread Aβ deposition in the form of plaques and cerebral amyloid angiopathy (Cohen et al., 2013) and to have early neurovascular dysfunction (Joo et al., 2017). All scanning was performed between the hours of 10.00am and 4.00pm across 9 days spanning a 2 month period. The time between scanning and culling was 4.6 ± 2.3 weeks (mean ± sd). All experimental procedures were approved by the Preclinical Imaging Executive Committee of the University of Manchester and carried out in accordance with the U.K Animals (Scientific Procedures) Act 1986 and EU Directive 2010/63/EU for animal experiments. Breeding, housing, and husbandry details, conforming to the ARRIVE guidelines (Kilkenny et al., 2010) can be found in supplementary materials.

1.2.4 MRI protocol

All rats were initially anesthetised with 4% isoflurane + 100% O_2 then maintained with 2-2.5% isoflurane + 100% O_2 for the duration of scanning. Scans were acquired on a Bruker Avance III console interfaced with an Agilant 7T 16cm bore magnet. A Bruker transmit only resonator (T11070V3) was used for transmission and a Bruker rat brain surface coil (T11205V3) was used for reception.

The image acquisition parameters are given in Table 1 and the protocol is shown in Figure 1. Axial T_1-RARE images were acquired using the scanner default parameters for the purpose of brain region delineation (Figure 1, dataset A). Coronal multi-flip angle spoiled gradient echo (SPGR) sequences were acquired at multiple TRs (long TR using 2D SPGR and short TR using 3D SPGR) to allow combined estimation of flip angle error (k) and pre-contrast T_1in blood and each brain region (Figure 1; dataset B). For short TR data, 10 gradient echoes were acquired per RF excitation to allow correction for T_2* decay. Dynamic SPGR acquisitions (Figure 1, datasets C and E) were collected for estimation of trans-BBB contrast agent leakage rate, K^{trans}. These scans had a short TR to *minimize* sensitivity to τ_b, and high spatial resolution to enable sampling of blood signal from the superior sagittal sinus (SSS), free from partial volume effects. Gadoteric acid (Dotarem, Guerbet; dose = 0.5 mmol kg^{-1}) was injected intravenously on the 6th volume of dataset C through a 24G cannular inserted into the tail vein with a pump at 1 mL min^{-1}. After equilibration of the contrast agent throughout the blood pool (at approximately 2.5 minutes following first pass), dataset D was collected to estimate PS_w. Dataset D had a long TR, large voxels, and multiple repetitions, to *maximize* sensitivity to τ_b. Multiple flip angles were used to provide differential sensitivity to p_b and τ_b, as shown in Figure 3a-b. The slice/slab select direction was placed along the superior-inferior direction (coronal slices) to ensure non-selective excitation of spins along the rostral-caudal direction to minimize T_1 inflow effects.

1.2.5 Analysis pipeline

The data analysis pipeline is shown in Figure 2. Signals were corrected for T_2* decay by fitting a mono-exponential decay model to multi-gradient echo data (Figure 2a), providing estimates of the signal magnitude at zero echo time, S(TE = 0). Flip angle error ($k = \alpha/\alpha_0$, where α is the delivered flip angle, and α_0 the prescribed flip angle at the scanner console) and pre-contrast T_1 were mapped voxel-wise by jointly fitting SPGR signal models to multi-TR multi-flip angle data (Dickie et al., 2015;

Voigt et al., 2010) (Figure 2b). Linear interpolation was used to up-sample long TR data to the matrix size of the short TR data. MRI signals from hippocampal, cortical, striatal, and thalamic regions were extracted for each rat by registering the high resolution T_1-RARE image (Figure 1; dataset A) to the Schwarz et al. rat brain atlas (Schwarz et al., 2006). Image registration was performed using in-house software written in Matlab (The Mathworks, Inc., Natick, Massachusetts, USA). Regional estimates of k, T_1, and S(TE = 0) were obtained by taking the median from voxels in the region. Regional estimates of PS_w were then obtained by fitting SPGR signal models for an exchanging two-site system (Buckley et al., 2008) to regional multi-flip angle decay-corrected signals from dataset D:

$$S(TE=0,t) = S_0\left[a_s(t)\frac{\sin\alpha\left(1-e^{\frac{-TR}{T_{1,S}(t)}}\right)}{\left(1-\cos\alpha\, e^{\frac{-TR}{T_{1,S}(t)}}\right)} + (1-a_s(t))\frac{\sin\alpha\left(1-e^{\frac{-TR}{T_{1,L}(t)}}\right)}{\left(1-\cos\alpha\, e^{\frac{-TR}{T_{1,L}(t)}}\right)}\right] \quad (3)$$

where S(TE = 0, t) is the MRI signal at zero echo time (TE = 0) as a function of acquisition time, t, $a_S(t)$ is the apparent blood water population fraction, $T_{1,S}(t)$ is the apparent intravascular T_1 value in the presence of trans-BBB water exchange, and $T_{1,L}(t)$ is the apparent extravascular T_1 value in the presence of trans-BBB water exchange, α is the delivered flip angle ($\alpha = k\alpha_0$), and TR is the repetition time. The two-site one-exchange (2S1X) model solutions relate a_s, $T_{1,S,}$ and $T_{1,L}$ to the true blood water population fraction p_b, the mean blood water residence time τ_b, and true intravascular and extravascular T_1 values ($T_{1,b}$ and $T_{1,e}$, respectively) (Landis et al., 1999):

$$a_s = \frac{1}{2} - \frac{1}{2}\left(\frac{\left[\left(\frac{1}{T_{1,e}} - \frac{1}{T_{1,b}(t)}\right)(2p_b-1) + \frac{p_b}{(1-p_b)\tau_b} + \frac{1}{\tau_b}\right]}{\left[\left(\frac{1}{T_{1,e}} - \frac{1}{T_{1,b}(t)} + \frac{p_b}{(1-p_b)\tau_b} - \frac{1}{\tau_b}\right)^2 + \frac{4p_b}{(1-p_b)\tau_b^2}\right]^{\frac{1}{2}}}\right) \quad (4)$$

$$\frac{1}{T_{1,S}(t)} = \frac{1}{2}\left[\left(\frac{1}{T_{1,e}} + \frac{1}{T_{1,b}(t)} + \frac{p_b}{(1-p_b)\tau_b} + \frac{1}{\tau_b}\right) + \left[\left(\frac{1}{T_{1,e}} - \frac{1}{T_{1,b}(t)} + \frac{p_b}{(1-p_b)\tau_b} - \frac{1}{\tau_b}\right)^2 + \frac{4p_b}{(1-p_b)\tau_b^2}\right]^{\frac{1}{2}}\right] \quad (5)$$

$$\frac{1}{T_{1,L}(t)} = \frac{1}{2}\left[\left(\frac{1}{T_{1,e}} + \frac{1}{T_{1,b}(t)} + \frac{p_b}{(1-p_b)\tau_b} + \frac{1}{\tau_b}\right) - \left[\left(\frac{1}{T_{1,e}} - \frac{1}{T_{1,b}(t)} + \frac{p_b}{(1-p_b)\tau_b} - \frac{1}{\tau_b}\right)^2 + \frac{4p_b}{(1-p_b)\tau_b^2}\right]^{\frac{1}{2}}\right] \quad (6)$$

The T_1 relaxation time of extravascular water, $T_{1,e}$, was fixed to its pre-contrast value, effectively enforcing an assumption of zero contrast agent leakage across the BBB. Before injection of the contrast agent, we assume the fast-exchange limit holds and thus parametrise $T_{1,e}$ in terms of pre-

contrast blood and tissue T_1 values ($T_{1,b}(t=0)$ and $T_{1,t}(t=0)$), which were estimated through pre-contrast T_1 mapping, and p_b, which was unknown at the time of fitting:

$$T_{1,e} = \frac{(1 - p_b)}{\left(\frac{1}{T_{1,t}(t=0)} - \frac{p_b}{T_{1,b}(t=0)}\right)} \quad (7)$$

The T_1 relaxation time of blood, $T_{1,b}(t)$, was estimated via the following expression:

$$\frac{1}{T_{1,b}(t)} = \frac{1}{T_{1,b}(t=0)} + r_1 C_b(t) \quad (8)$$

where r_1 is the T_1 relaxivity of gadoteric acid, set to 3.5 $(mM\ s)^{-1}$ (Rohrer et al., 2005). $T_{1,b}(t = 0)$ and $C_b(t)$, and thus $T_{1,b}(t)$, were measured from the superior sagittal sinus (SSS) using datasets B, C and E. SSS voxels were chosen as follows. A slice containing the SSS was manually selected from the 4th post-contrast volume (SSS appears bright). A histogram of decay-corrected signals from this slice was generated and voxels with S(TE = 0) in the 99th percentile of all signals in the slice were selected. Quality control checks were performed to ensure these voxels did indeed arise from the SSS, and not from other vessels in the brain. Pre-contrast T_1 of blood, $T_{1,b}(t = 0)$, was estimated from dataset B by taking the median T_{1b} value from selected SSS voxels. $C_b(t)$ was estimated from the median SSS signal acquired during C and E, using knowledge of $T_{1,b}(t = 0)$ estimated from dataset B. During dataset D, $C_b(t)$ was not measured directly, but inferred from a bi-exponential fit to $C_b(t)$ measured in C and E (Figure 2d). Therefore, the only unknowns during fitting of Eqn. 3 to dataset D were p_b, τ_b, and S_0.

Estimates of the permeability surface-area product to water, PS_w, were obtained from the ratio of p_b and τ_b, scaled by the brain-blood partition coefficient for water, λ. We assumed λ is uniform across the brain and equal to 0.9 (Herscovitch and Raichle, 1985). The trans-BBB leakage rate of contrast agent, K^{trans}, was estimated by fitting the Patlak model (Patlak et al., 1983) to datasets C and E. To reproduce Patlak model analyses present in the literature (Montagne et al., 2015; van de Haar et al., 2016) blood and tissue concentrations were derived from the first gradient echo (TE = 2.09 ms), not the decay corrected signal. All model fitting was done in statistical software package R (Version 3.1, R Foundation for Statistical Computing, Vienna, Austria).

The noise-to-signal ratio of extracted curves was estimated in five randomly selected rats and used to infer parameter CoV using results from Monte Carlo simulations. Noise-to-signal ratio was estimated by dividing the standard deviation of signal, computed from the first six flip angle images of dataset D, by the equilibrium signal (S_0) estimated from model fitting. Using the measured noise-to-signal ratios, the parameter CoV was inferred using the data from Figure 3d as a look-up table.

1.2.6 Post-hoc protocol appraisal

To evaluate possible time-saving modifications to our imaging protocol, Eqn. 3 was re-fitted to dataset D using only 2 or 3 of the 6 available repeats collected for each flip angle. Bland-Altman plots showing the difference in parameter estimates were generated and the null hypothesis of no differences in the mean and variance of parameter estimates tested using t- and F-tests, respectively.

1.2.7 Immunofluorescent staining, imaging, and quantification

Following MRI, the brains of all animals were collected and underwent immunohistochemistry to visualize proteins linked to the tight junctions (occludin, claudin-5) and membrane water channels (aquaporin-4). All proteins were dual stained with lectin to visualize vessels. Slides were imaged at 40x using a 3D Histech Pannoramic P250 Flash slide scanner and the area of staining quantified

using in-house software. In transgenic rats, lectin led to aspecific staining of amyloid-β plaques. No amyloid-β staining was observed in wild-types. To avoid bias in derived statistics between TgF344-AD and wild-types, amyloid-β plaques were delineated manually on lectin images in ImageJ (v1.51, National Institute of Health, USA) and excluded from quantification of lectin and marker expression. Full details of immunohistochemistry, slide imaging, and quantification are given in supplementary materials.

1.2.8 Statistical analysis of MRI and immunofluorescent data

Two way analysis of variance (ANOVA) with effects of genotype and region (plus the genotype-region interaction) were performed on estimates of PS_w, K^{trans}, and all immunostains. Region was input as a repeated measure. Based on the ANOVA results, PS_w and K^{trans} measures were correlated against occludin (% snapshot area), i) in each brain region ignoring group status, ii) averaging PS_w, K^{trans}, and occludin across the four brain regions and computing independent correlations for TgF344-AD and wildtype rats. Correlation coefficients were tested for statistical significance against the null hypothesis of zero correlation. All statistical analyses were done in R (Version 3.1, R Foundation for Statistical Computing, Vienna, Austria). No corrections were made for multiple comparisons.

1.3 Results

1.3.1. Sensitivity analysis

Our simulations show τ_b and p_b sensitivity varies with both excitatory flip angle (α) and repetition time (TR) (Figure 3a-b). In both cases, sensitivity profiles for p_b and τ_b diverge, suggesting either approach (varying flip angle, or varying TR) could be used to estimate these parameters from MRI data. Sensitivity to τ_b was maximum at intermediate flip angles and at longer TRs. Sensitivity to p_b was maximum at large flip angles and short TRs. Sensitivity to τ_b was near zero at low blood contrast agent concentrations (C_b ~ 0), and increased linearly with C_b up to approximately 4mM, after which sensitivity increased more slowly (Figure 3c). Sensitivity to p_b plateaued at a lower C_b than τ_b.

1.3.2. Monte Carlo Simulations

In MFAME-MRI, we opt to vary flip angle, while using a relatively long, fixed TR (100 ms), such that T_2* decay can be quantified and corrected in all images using an invariant multi-gradient echo readout. Figure 3d shows how the CoV in PS_w is reduced by using more unique flip angles rather than acquiring more repeats of the same flip angles, up to approximately 5 angles, after which CoV does not decrease further. In MFAME-MRI we use 5 flip angles centred around 30º. The highest flip angle is increased from 50º to 80º to obtain a single image with very high sensitivity to p_b but low sensitivity to τ_b (see Figure 3a).

Simulations showed that flip angle error caused by B_1^+ field inhomogeneity produces substantial biases in all parameters (black lines in Figure 3e). Estimating flip angle error directly from multi-TR multi-flip angle data, alongside pre-contrast T_1, successfully removed these biases (overlapping red lines in Figure 3e). This correction method was implemented in the rat experiments. Non-zero K^{trans} caused overestimation of p_b and τ_b, however, because PS_w is the ratio of these measures, it was mostly unaffected (< 8% bias up to $K^{trans} = 10^{-3}$ min^{-1}; Figure 3f).

1.3.3 Animal experiments

ANOVA analyses revealed that PS_w differed between genotype ($p = 0.0022$; higher PS_w in TgF344-AD rats), but not between brain region ($p = 0.93$) (Figure 4a). There was no genotype-region interaction effect ($p = 0.85$). While ANOVA analyses suggest the magnitude of PS_w alterations are not region dependent (between the regions studied), the plotted data in Figure 4a show that the largest changes occur in the hippocampus, striatum and thalamus, with the smallest effect in the cortex. The trans-BBB leakage rate of MRI contrast agent (K^{trans}) did not differ significantly between transgenic and

wild-type animals ($p = 0.477$) or between brain region ($p = 0.226$), and had no genotype-region interaction ($p = 0.97$) (Figure 4b).

As PS_w was hypothesized to be closely related to BBB integrity, we assessed by immunohistochemistry vessel area by lectin and the expression of three different BBB markers: two tight junction proteins (occludin and claudin-5) and a water channel protein (aquaporin-4). ANOVA analyses revealed a genotype effect for occludin ($p = 0.0061$), but no region effect ($p = 0.64$) or genotype-region interaction ($p = 0.92$). Claudin-5 and aquaporin-4 did not display any genotype ($p = 0.58$ and $p = 0.73$ respectively), region ($p = 0.070$ and $p = 0.38$ respectively), or genotype-region interaction effects ($p = 0.32$ and $p = 0.43$ respectively – Figures 4e-f). Vessel area as quantified by lectin staining did not differ significantly between transgenic and wild-types ($p = 0.27$, Figure 4g), but did differ between brain region ($p < 3 \times 10^{-5}$). Region specific correlation analyses showed that rats with lower occludin had higher PS_w (Figure 4h). In these plots, correlations were driven by both within- and between-group variability. Because vessel area assessed by lectin did not differ significantly between genotype, genotype differences in occludin and PS_w were most likely due to altered expression of the protein per unit vessel length (and therefore indicative of reduced BBB integrity), and not due to reduced vessel surface area or density. When estimates of PS_w and occludin were averaged across the four brain regions and each group treated independently, correlations remained statistically significant (Figure 4i) indicating that PS_w is sensitive to natural occludin variation present within both TgF344-AD and wild-type groups. K^{trans} did not correlate with occludin.

The noise-to-signal ratios of *in-vivo* regional multi-flip angle curves were between 0.001-0.003 (corresponding to signal-to-noise ratios of 333-1000). Using the data presented in Figure 3d as a look-up table, these noise-to-signal ratios gave predicted *in-vivo* parameter CoV values of 10-20% for p_b, 10-30% for τ_b, and 15-45% for PS_w, dependent on brain region. Noise-to-signal ratios, and thus predicted CoV values, were largest for the hippocampus, and smallest for the cortex.

Figure 5 shows the results of the post hoc protocol appraisal. Estimating PS_w using only two of the six available image repeats collected for dataset D did not significantly alter the central tendency (mean) ($p = 0.22$) or variance (precision) ($p = 0.80$) of PS_w estimates. Using 3 repeats also led to similar results ($p = 0.21$ and $p = 0.22$).

1.4 Discussion

BBB breakdown is known to occur with ageing and could be exacerbated in AD, accelerating disease pathogenesis and associated cognitive decline (Sweeney et al., 2018; Zlokovic, 2011). While a number of studies have shown an interaction between Aβ and tight junction proteins (Keaney et al., 2015; Kook et al., 2012), the impact of AD pathology on BBB breakdown has been difficult to robustly demonstrate *in-vivo*. A recent study evaluating BBB disruption in a variety of AD mouse models failed to detect AD-related differences in the blood-brain leakage of injected probes (Bien-Ly et al., 2015). A meta-analysis of cerebrospinal fluid assay and imaging studies also failed to infer a statistically significant effect of AD on BBB integrity (Farrall and Wardlaw, 2009). However, recent prospective human studies using advanced dynamic contrast-enhanced MRI have been able to detect increased leakage of contrast agent across the BBB in patients with mild-cognitive impairment (Montagne et al., 2015) and in early AD (van de Haar et al., 2016), supporting an argument for AD-related BBB damage. In our study of the TgF344-AD rat model, we fail to detect any increase in BBB permeability to MRI contrast agent, but do detect increased permeability to water, indicating MFAME-MRI may be more sensitive than available 'tracer leakage' methods and could provide a more useful marker of subtle BBB breakdown.

The consequence of subtle BBB damage is unknown. It is unlikely to impact the trans-BBB transport of large molecules. More likely is that such changes (i.e., increased water-exchange) will impact ion homeostasis and brain water balance (Amiry-Moghaddam and Ottersen, 2003) which is required for proper functioning of neuronal circuits. Furthermore, if BBB damage is a crucial early event in AD

pathogenesis, methods such as those presented here will be extremely useful for studying the timing and order of BBB changes when they first occur, and possibly for monitoring the response of novel BBB-targeted therapeutics.

The overall measurement time used in this study was long, presenting a potential barrier for implementation of this exact protocol to scan human patients with dementia. Figure 1 shows scan time is approximately split between pre-contrast B_1^+-T_1 mapping and post-contrast measurements. In a clinical setting, less time-consuming flip angle mapping approaches based on Bloch-Siegert shift could be used (Sacolick et al., 2010). Examination of Figure 3b shows reductions in TR could be implemented, reducing down to 75 or 50 ms, with little effect on the precision of τ_b. Such changes may actually increase precision in PS_w through increased sensitivity to p_b, however simulations are required to test this hypothesis. Furthermore, additional time saving modifications to our method may be gained by acquiring fewer repetitions per unique flip angle, which we show does not significantly alter the central tendency or precision of PS_w estimates. Last, since MFAME-MRI uses multiple flip angles to gain PS_w sensitivity and multiple TRs for estimation of flip angle error, reductions in scan time may also be gained by using an MR fingerprinting approach (Ma et al., 2013).

Our approach uses standard MRI contrast agents, which leak across the BBB unless the BBB is fully intact. The modelling used here to estimate PS_w assumes that no leakage occurs, which may not be true due to age- (Montagne et al., 2015) or cerebrovascular disease (Farrall and Wardlaw, 2009) related BBB breakdown. However, we show that at the leakage levels expected in dementia patients (10^{-5} – 10^{-3} min^{-1}), and for those levels measured in TgF344-AD rats in this study (~1-3 x 10^{-4} min^{-1}), leakage of contrast agent does not substantially impact estimates of PS_w (Figure 3f). Furthermore, it may still be possible to use our MFAME-MRI approach in stroke or tumours where leakage of contrast agent is greater, however a generalised water-exchange model that accounts for non-zero K^{trans} would be required (Li et al., 2005). Other MRI approaches have been proposed for quantifying trans-BBB water-exchange which do not rely on injection of exogenous tracers; e.g. diffusion-weighted arterial spin labelling MRI (Silva et al., 1997; St. Lawrence et al., 2012). However, these techniques are usually limited to estimation of τ_b, which is likely to be a less physiologically specific measure of BBB integrity due to its co-dependence on both PS_w and p_b.

The study had the following limitations. Aspecific staining of amyloid plaques was observed in lectin immuno-stains of transgenic rats, but not in wildtypes. Since such plaques were large in size relative to vessels (see Figure 4c and Supplementary Figure 1), the snapshot image area covered by such plaques was removed from analyses, and snapshot statistics adjusted accordingly. If amyloid plaques were present in regions of highest or lowest vessel density, it is possible that such a procedure could have biased quantification of lectin, occludin, claudin-5, and aquaporin-4, artificially reducing or increasing the '% of snapshot' quantified respectively, relative to wild-types. However, we did not see a favoured pattern of amyloid deposition visually, and believe that such biasing is unlikely. Aspecific staining of vascular amyloid may have also occurred in lectin immuno-stains, however due to the proximity of vascular amyloid deposits to the vessel lumen, it was not possible to ascertain if this was present, and if so correct for it. Such staining, if non-negligible, would have led to an artefactual increase in the amount of lectin classified as vessel in TgF344-AD rats, relative to wild-types. The animals used were relatively old (~18 months). Their age at time of scanning was chosen primarily to maximise the severity of AD pathology and thus AD-related BBB damage. It is possible that age-related BBB damage may also have been present, which would also have presented in wild-types, and could be a possible explanation for some of the within-group variation that is observed, particularly in the wild type animals. The relative magnitude of age and AD-related BBB damage is currently unknown and should be investigated in future studies, both in animal models and humans. The rats were not culled immediately following scanning. Some BBB damage may have occurred between scanning and culling, which may have added variability to MRI and immunohistochemistry comparisons, worsening correlations. However, since the time delay was only a small fraction of the entire lifetime of the animal, we expect this effect to be minimal.

In summary, we have demonstrated MFAME-MRI can non-invasively detect subtle BBB permeability alterations in a rat model of AD, related to decreased expression of the BBB tight junction protein occludin. Until now, MRI techniques have focused on measuring the leakage of hydrophilic passively dispersed exogenous probes. However, when BBB breakdown is subtle, as may be the case in AD, such probes leak very slowly, resulting in low measurement sensitivity. MFAME-MRI is a new promising tool to study subtle BBB damage, potentially enabling detection of cerebrovascular pathology far earlier in disease pathogenesis than previously possible.

1.5 Data availability statement

The data that support the findings of this study are available from the corresponding author upon reasonable request.

1.6 Acknowledgments

The authors would like to thanks Mrs Lidan Christie and Karen Davies for their technical contribution.

1.7 Funding

The purchase of the TgF344-AD rat was jointly supported by the European Union's Seventh Framework Programme (FP7/2007-2013) under grant agreement n° HEALTH-F2-2011-278850 (INMiND) and Alzheimer Research UK network funds. The breeding and maintenance of the TgF344-AD rat was supported by the European Union's Seventh Framework Programme (FP7/2007-2013) under grant agreement n° HEALTH-F2-2011-278850 (INMiND). BD, MV as well as scanning of the TgF344-AD rats were funded by the EPSRC project EP/M005909/1. The MRI facility is supported through an equipment grant from BBSRC UK (BB/F011350).

1.8 Author Contributions

BD designed the MRI protocol, acquired the imaging data, and performed data analysis and statistics. JU contributed to MRI protocol development and optimisation. MV performed immunostaining. GP, LP and HB supervised the work and contributed to preparation of the manuscript.

1.9 Competing Interest Statement

GJMP is a shareholder and director of Bioxydyn Limited, a company with an interest in quantitative imaging biomarkers

1.10 Figure Legends

Figure 1. The MRI protocol. Dataset A: high resolution T_1-RARE images for segmentation of key brain regions in conjunction with the Schwarz et al. rat atlas. Dataset B: multi-repetition time (TR) multi-flip angle spoiled gradient recalled echo (SPGR) images for combined flip angle error (k) and pre-contrast T_1 mapping. Datasets C and E: high spatial resolution dynamic SPGR images for estimation of K^{trans} and monitoring contrast agent concentration in the superior sagittal sinus (SSS). Dataset D: low spatial resolution multi-flip angle multi-echo (MFAME)-MRI SPGR images for estimation of PS_w. Abbreviations: CA, contrast agent; k, flip angle error; TR, repetition time; TE, echo time; n_{rep}, number of image repetitions.

Figure 2. Analysis pipeline for estimation of PS_w and K^{trans}. **a** A mono-exponential model is fit to multi-gradient echo signals to correct for T_2* decay, producing estimates of MRI signal at zero echo time, S(TE = 0). **b** Maps of flip angle error (k) and pre-contrast T_1 are estimated from short TR (red points) and long TR (black points) data by jointly fitting the spoiled gradient echo (SPGR) signal model, assuming the fast exchange limit for water exchange. Red and black lines show the joint fit to this data. **c** Median MRI signals, k and T_1 for each region are extracted by registering the T_1–weighted

RARE anatomic image to the Schwarz et al. atlas. Blood signals and associated k and T_1 values are extracted from the superior sagittal sinus (SSS) using a semi-automated procedure. **d** A bi-exponential model is fit to measurements of blood contrast agent concentration (C_b) from datasets C and E. The model fit is used to infer C_b during dataset D. **e** The two-site one-exchange (2S1X) model is fit to regional tissue curves from dataset D to estimate the mean blood water residence time (τ_b), blood water population fraction (p_b), and the trans-BBB permeability surface area product to water (PS_w). **f** The Patlak model is fit to regional tissue curves from datasets C and E to estimate the trans-BBB leakage rate of contrast agent, K^{trans}. In a, b, d, e, and f, data points and fitted curves are representative of the signal to noise ratio and fit quality of acquired rat data.

Figure 3. Sensitivity analysis and Monte Carlo simulations. **a-c** Sensitivity plots showing the percentage increase or decrease in post-contrast MRI signal intensity due to a 50% increase in τ_b (solid line) or p_b (dashed line) as a function of flip angle, TR, and blood contrast agent concentration (C_b). The dotted line denotes zero change in signal. **d** Coefficient of variation (CoV) of p_b, τ_b, and PS_w estimates (dotted line) as a function of noise-signal ratio for different unique flip angle and image repeat combinations estimated from Monte Carlo simulations. Noise sd is the standard deviation of zero mean Gaussian noise, S_0 is the equilibrium signal. Symbols indicate the noise-to-signal ratio of *in-vivo* rat data acquired with $n_\alpha = 5$ (* = hippocampus; + = cortex, $ = striatum, # = thalamus). **e** The effect of flip angle error ($k = \alpha/\alpha_0$) on p_b, τ_b, and PS_w when assuming the delivered flip angle (α) is equal to the prescribed flip angle (α_0) (black lines). The overlapping red lines show bias in parameter estimates following flip angle error correction using multi-TR multi-flip angle data. **f** The effect of non-zero K^{trans} on p_b, τ_b, and PS_w.

Figure 4. MRI and immunostaining results in TgF344-AD and wild-type rats. **a** PS_w is significantly higher (up to 2-fold) in TgF344-AD rats relative to wild-types ($p < 0.05$; two-way ANOVA). **b** Trans-BBB leakage of contrast agent (K^{trans}) is unaltered between TgF344-AD rats and wild-types ($p = 0.477$; two-way ANOVA). **c** Representative occludin and lectin immuno-stains. Aspecific staining of amyloid-β was visually identified on the lectin snapshots and manually segmented as shown. Segmented regions were then removed from the calculation of snapshot statistics. **d** Occludin is reduced in TgF344-AD relative to wild-types ($p < 0.05$; two-way ANOVA), corresponding well with genotype differences in PS_w. **e** No detectable TgF344AD/wild-type differences were observed for claudin-5 or, **f** aquaporin-4 (AQP4). **g** Lectin stains showed no difference in total vessel area between TgF344-AD and wild-types ($p = 0.27$; two-way ANOVA). **h** PS_w measurements correlated inversely with occludin staining in all regions tested. **i** When estimates for each rat were averaged across the four regions, and group-wise correlations computed, correlations maintained significance, confirming that occludin can explain variability in PS_w independent of group. In h-i, black markers represent TgF344-AD rats and white markers represent wild-types. In all plots, '% of snapshot' is the percentage area of snapshot occupied by the immunostain, averaged across all snapshots taken for that region. Data shown in a, b, d, e, f, and g are mean ± s.e.m.

Figure 5. Post-hoc protocol appraisal. Bland-Altman plots show the difference in PS_w estimates (ΔPS_w) when fitting to dataset D with 6 versus 2 repetitions per flip angle. In all regions, the use of 2 repetitions underestimated PS_w relative to 6 repetitions, but differences were not statistically significant ($p = 0.22$). Variance in PS_w across both groups was also unaltered ($p = 0.80$). Black dots represent TgF344-AD rats, while white dots represent wild-types. The solid dotted lines denotes $\Delta PS_w = 0$, while the dotted horizontal lines denote the mean bias in ΔPS_w between estimates using 6 vs 2 repeats.

Supplementary Figure 1. Representative claudin-5 and aquaporin-4 immuno-stains, and an example of lectin segmentation. **a** Representative claudin-5 and lectin immuno-stains. **b** Representative aquaporin-4 and lectin immuno-stains. Aspecific staining of amyloid-β was visually identified on the lectin snapshots and manually segmented. Segmented regions were then removed from calculation of snapshot statistics. **c** An image of an entire sagittal section stained with lectin. Each animal had 4

such sections cut at different locations from bregma. The white box shows the relative size of 10x snapshot images taken in the cortex, compared to the overall size of the section. **d** The corresponding 10x lectin image shown in c **e** The segmentation image derived by passing the lectin image in d through the in-house segmentation pipeline.

1.11 Bibliography

Amiry-Moghaddam, M., Ottersen, O.P., 2003. The molecular basis of water transport in the brain. Nat. Rev. Neurosci. 4, 991–1001. https://doi.org/10.1038/nrn1252

Armitage, P.A., Farrall, A.J., Carpenter, T.K., Doubal, F.N., Wardlaw, J.M., 2011. Use of dynamic contrast-enhanced MRI to measure subtle blood–brain barrier abnormalities. Magn. Reson. Imaging 29, 305–314. https://doi.org/10.1016/j.mri.2010.09.002

Bains, L.J., McGrath, D.M., Naish, J.H., Cheung, S., Watson, Y., Taylor, M. Ben, Logue, J.P., M. Parker, G.J., Waterton, J.C., Buckley, D.L., 2010. Tracer kinetic analysis of dynamic contrast-enhanced MRI and CT bladder cancer data: A preliminary comparison to assess the magnitude of water exchange effects. Magn. Reson. Med. 603, n/a-n/a. https://doi.org/10.1002/mrm.22430

Bien-Ly, N., Boswell, C.A., Jeet, S., Beach, T.G., Hoyte, K., Luk, W., Shihadeh, V., Ulufatu, S., Foreman, O., Lu, Y., DeVoss, J., van der Brug, M., Watts, R.J., 2015. Lack of Widespread BBB Disruption in Alzheimer's Disease Models: Focus on Therapeutic Antibodies. Neuron 88, 289–297. https://doi.org/10.1016/j.neuron.2015.09.036

Brix, G., Kiessling, F., Lucht, R., Darai, S., Wasser, K., Delorme, S., Griebel, J., 2004. Microcirculation and microvasculature in breast tumors: pharmacokinetic analysis of dynamic MR image series. Magn. Reson. Med. 52, 420–429.

Buckley, D.L., Kershaw, L.E., Stanisz, G.J., 2008. Cellular-interstitial water exchange and its effect on the determination of contrast agent concentration in vivo: Dynamic contrast-enhanced MRI of human internal obturator muscle. Magn. Reson. Med. 60, 1011–1019. https://doi.org/10.1002/mrm.21748

Carrano, A., Hoozemans, J.J.M., van der Vies, S.M., Rozemuller, A.J.M., van Horssen, J., de Vries, H.E., 2011. Amyloid Beta Induces Oxidative Stress-Mediated Blood–Brain Barrier Changes in Capillary Amyloid Angiopathy. Antioxid. Redox Signal. 15, 1167–1178. https://doi.org/10.1089/ars.2011.3895

Caserta, M.T., Caccioppo, D., Lapin, G.D., Ragin, a, Groothuis, D.R., Caserta, Mt, Caccioppo, D, Lapin, Gd, 1998. Blood–brain barrier integrity in Alzheimer's disease patients and elderly control subjects. J. … 10, 78–84.

Cohen, R.M., Rezai-Zadeh, K., Weitz, T.M., Rentsendorj, A., Gate, D., Spivak, I., Bholat, Y., Vasilevko, V., Glabe, C.G., Breunig, J.J., Rakic, P., Davtyan, H., Agadjanyan, M.G., Kepe, V., Barrio, J.R., Bannykh, S., Szekely, C.A., Pechnick, R.N., Town, T., 2013. A Transgenic Alzheimer Rat with Plaques, Tau Pathology, Behavioral Impairment, Oligomeric A , and Frank Neuronal Loss. J. Neurosci. 33, 6245–6256. https://doi.org/10.1523/JNEUROSCI.3672-12.2013

Dickie, B.R., Banerji, A., Kershaw, L.E., Mcpartlin, A., Choudhury, A., West, C.M., Rose, C.J., 2015. Improved accuracy and precision of tracer kinetic parameters by joint fitting to variable flip angle and dynamic contrast enhanced MRI data. Magn. Reson. Med. 76, 1270–1281. https://doi.org/10.1002/mrm.26013

Donahue, K.M., Weisskoff, R.M., Burstein, D., 1997. Water diffusion and exchange as they influence contrast enhancement. J. Magn. Reson. Imaging 7, 102–110. https://doi.org/10.1002/jmri.1880070114

Dorr, A., Sahota, B., Chinta, L. V., Brown, M.E., Lai, A.Y., Ma, K., Hawkes, C.A., McLaurin, J., Stefanovic, B., 2012. Amyloid-β-dependent compromise of microvascular structure and function in a model of Alzheimer's disease. Brain 135, 3039–3050. https://doi.org/10.1093/brain/aws243

Farrall, A.J., Wardlaw, J.M., 2009. Blood–brain barrier: Ageing and microvascular disease – systematic review and meta-analysis. Neurobiol. Aging 30, 337–352. https://doi.org/10.1016/j.neurobiolaging.2007.07.015

Herscovitch, P., Raichle, M.E., 1985. What is the correct value for the brain--blood partition coefficient for water? J. Cereb. Blood Flow Metab. 5, 65–69. https://doi.org/10.1038/jcbfm.1985.9

Heye, A.K., Thrippleton, M.J., Armitage, P.A., Valdés Hernández, M. del C., Makin, S.D., Glatz, A., Sakka, E., Wardlaw, J.M., 2016. Tracer kinetic modelling for DCE-MRI quantification of subtle blood-brain barrier permeability. Neuroimage 125, 446–455. https://doi.org/10.1016/j.neuroimage.2015.10.018

Joo, I.L., Lai, A.Y., Bazzigaluppi, P., Koletar, M.M., Dorr, A., Brown, M.E., Thomason, L.A.M., Sled, J.G., Mclaurin, J., 2017. Early neurovascular dysfunction in a transgenic rat model of Alzheimer '

s disease. Nat. Publ. Gr. 1–14. https://doi.org/10.1038/srep46427
Keaney, J., Walsh, D.M., Malley, T.O., Hudson, N., Darragh, E., Loftus, T., Sheehan, F., Mcdaid, J., Humphries, M.M., Callanan, J.J., Brett, F.M., Farrell, M.A., Humphries, P., Campbell, M., 2015. Autoregulated paracellular clearance of amyloid-β across the blood-brain barrier. Sci Adv. 1, 1–24. https://doi.org/10.1126/sciadv.1500472.Autoregulated
Kilkenny, C.., Browne, W., Cuthill, I., Emerson, M., Altman, D., 2010. Animal research: Reporting in vivo experiments: The ARRIVE guidelines. Br. J. Pharmacol. 160, 1577–1579. https://doi.org/10.1113/expphysiol.2010.053793
Kook, S.-Y., Hong, H.S., Moon, M., Ha, C.M., Chang, S., Mook-Jung, I., 2012. A 1-42-RAGE Interaction Disrupts Tight Junctions of the Blood-Brain Barrier Via Ca2+-Calcineurin Signaling. J. Neurosci. 32, 8845–8854. https://doi.org/10.1523/JNEUROSCI.6102-11.2012
Landis, C.S., Li, X., Telang, F.W., Molina, P.E., Palyka, I., Vetek, G., Springer, C.S., 1999. Equilibrium transcytolemmal water-exchange kinetics in skeletal muscle in vivo. Magn. Reson. Med. 42, 467–478. https://doi.org/10.1002/(SICI)1522-2594(199909)42:3<467::AID-MRM9>3.0.CO;2-0
Li, X., Rooney, W.D., Springer, C.S., 2005. A unified magnetic resonance imaging pharmacokinetic theory: Intravascular and extracellular contrast reagents. Magn. Reson. Med. 54, 1351–1359. https://doi.org/10.1002/mrm.20684
Ma, D., Gulani, V., Seiberlich, N., Liu, K., Sunshine, J.L., Duerk, J.L., Griswold, M.A., 2013. Magnetic resonance fingerprinting. Nature 495, 187–192. https://doi.org/10.1038/nature11971
Montagne, A., Barnes, S.R., Sweeney, M.D., Halliday, M.R., Sagare, A.P., Zhao, Z., Toga, A.W., Jacobs, R.E., Liu, C.Y., Amezcua, L., Harrington, M.G., Chui, H.C., Law, M., Zlokovic, B. V., 2015. Blood-Brain barrier breakdown in the aging human hippocampus. Neuron 85, 296–302. https://doi.org/10.1016/j.neuron.2014.12.032
Montagne, A., Nation, D.A., Sweeney, M.D., Toga, A.W., 2016. Brain imaging of neurovascular dysfunction in Alzheimer's disease. Acta Neuropathol. https://doi.org/10.1007/s00401-016-1570-0
Patlak, C.S., Blasberg, R.G., Fenstermacher, J.D., 1983. Graphical evaluation of blood-to-brain transfer constants from multiple-time uptake data. J. Cereb. Blood Flow Metab. 3, 1–7. https://doi.org/10.1038/jcbfm.1985.87
Rohrer, M., Bauer, H., Mintorovitch, J., Requardt, M., Weinmann, H.-J., 2005. Comparison of magnetic properties of MRI contrast media solutions at different magnetic field strengths. Invest. Radiol. 40, 715–724. https://doi.org/10.1097/01.rli.0000184756.66360.d3
Sacolick, L.I., Wiesinger, F., Hancu, I., Vogel, M.W., 2010. B 1 mapping by Bloch-Siegert shift. Magn. Reson. Med. 63, 1315–1322. https://doi.org/10.1002/mrm.22357
Schlageter, N.L., Carson, R.E., Rapoport, S.I., 1987. Examination of blood-brain barrier permeability in dementia of the Alzheimer type with [68Ga]EDTA and positron emission tomography. J. Cereb. Blood Flow Metab. 7, 1–8. https://doi.org/10.1038/jcbfm.1987.1
Schwarz, A.J., Danckaert, A., Reese, T., Gozzi, A., Paxinos, G., Watson, C., Merlo-Pich, E. V., Bifone, A., 2006. A stereotaxic MRI template set for the rat brain with tissue class distribution maps and co-registered anatomical atlas: Application to pharmacological MRI. Neuroimage 32, 538–550. https://doi.org/10.1016/j.neuroimage.2006.04.214
Schwarzbauer, C., Morrissey, S.P., Deichmann, R., Hillenbrand, C., Syha, J., Adolf, H., Nöth, U., Haase, A., 1997. Quantitative magnetic resonance imaging of capillary water permeability and regional blood volume with an intravascular {MR} contrast agent. Magn Reson Med 37, 769–777.
Silva, A.C., Williams, D.S., Koretsky, A.P., 1997. Evidence for the exchange of arterial spin-labeled water with tissue water in rat brain from diffusion-sensitized measurements of perfusion. Magn. Reson. Med. 38, 232–7. https://doi.org/10.1002/mrm.1910380211
St. Lawrence, K.S., Owen, D., Wang, D.J.J., 2012. A two-stage approach for measuring vascular water exchange and arterial transit time by diffusion-weighted perfusion MRI. Magn. Reson. Med. 67, 1275–1284. https://doi.org/10.1002/mrm.23104
Starr, J.M., Farrall, A.J., Armitage, P., McGurn, B., Wardlaw, J., 2009. Blood-brain barrier permeability in Alzheimer's disease: a case-control MRI study. Psychiatry Res. 171, 232–241. https://doi.org/10.1016/j.pscychresns.2008.04.003
Sweeney, M.D., Sagare, A.P., Zlokovic, B. V., 2018. Blood-brain barrier breakdown in Alzheimer disease and other neurodegenerative disorders. Nat. Rev. Neurol. 14, 133–150. https://doi.org/10.1038/nrneurol.2017.188
van de Haar, H.J., Burgmans, S., Hofman, P.A.M., Verhey, F.R.J., Jansen, J.F.A., Backes, W.H., 2014. Blood-brain barrier impairment in dementia: Current and future in vivo assessments. Neurosci. Biobehav. Rev. 49C, 71–81. https://doi.org/10.1016/j.neubiorev.2014.11.022

van de Haar, H.J., Burgmans, S., Jansen, J.F.A., van Osch, M.J.P., van Buchem, M.A., Muller, M., Hofman, P.A.M., Verhey, F.R.J., Backes, W.H., 2016. Blood-Brain Barrier Leakage in Patients with Early Alzheimer Disease. Radiology 281, 527–535. https://doi.org/10.1148/radiol.2016152244

Vinters, H. V, 1987. Cerebral amyloid angiopathy. A critical review. Stroke. 18, 311–24. https://doi.org/10.1161/01.STR.18.2.311

Voigt, T., Nehrke, K., Doessel, O., Katscher, U., 2010. T1 corrected B1 mapping using multi-TR gradient echo sequences. Magn. Reson. Med. 64, 725–733. https://doi.org/10.1002/mrm.22333

Wang, Z., Su, M.Y., Nalcioglu, O., 1998. Measurement of tumor vascular volume and mean microvascular random flow velocity magnitude by dynamic Gd-DTPA-albumin enhanced and diffusion-weighted MRI. Magn. Reson. Med. 40, 397–404. https://doi.org/10.1002/mrm.1910400309

Weller, R.O., Subash, M., Preston, S.D., Mazanti, I., Carare, R.O., 2008. Perivascular drainage of amyloid-β peptides from the brain and its failure in cerebral amyloid angiopathy and Alzheimer's disease. Brain Pathol. 18, 253–266. https://doi.org/10.1111/j.1750-3639.2008.00133.x

Yarnykh, V.L., 2007. Actual flip-angle imaging in the pulsed steady state: A method for rapid three-dimensional mapping of the transmitted radiofrequency field. Magn. Reson. Med. 57, 192–200. https://doi.org/10.1002/mrm.21120

Zhang, X., Petersen, E.T., Ghariq, E., De Vis, J.B., Webb, A.G., Teeuwisse, W.M., Hendrikse, J., Van Osch, M.J.P., 2013. In vivo blood T1 measurements at 1.5 T, 3 T, and 7 T. Magn. Reson. Med. 70, 1082–1086. https://doi.org/10.1002/mrm.24550

Zlokovic, B. V., 2011. Neurovascular pathways to neurodegeneration in Alzheimer's disease and other disorders. Nat. Rev. Neurosci. 12, 723–739. https://doi.org/10.1038/nrn3114

Table 1. MFAME-MRI acquisition parameters.

	Dataset					
	A	***B (long TR)***	***B (short TR)***	***C***	***D***	***E***
Pulse sequence	T_1w RARE	SPGR	Multi-echo SPGR	Multi-echo SPGR	Multi-echo SPGR	Multi-echo SPGR
Orientation	Axial	Coronal	Coronal	Coronal	Coronal	Coronal
Acquisition type	2D	2D	3D	3D	3D	3D
Flip angle (º)	90	5, 10 20, 30, 40, 60, 80, 90	5, 10, 40, 60	60	30, 40, 20, 10, 80	60
TR (ms)	1500	5000	100	20	100	20
TE (ms)	7	2.1	2.1	2.1	2.1	2.1
ΔTE (ms)	N/A	N/A	2.1	2.1	2.1	2.1
# gradient echoes	N/A	1	10	6	10	6
FOV (mm)	30 x 30 x 30	30 x 30 x 30	30 x 30 x 30	30 x 30 x 30	30 x 30 x 30	30 x 30 x 30
Acquired Matrix size	256 x 256	32 x 16	64 x 32 x 48	64 x 32 x 48	32 x 16 x 16	64 x 32 x 48
Reconstructed Matrix size	256 x 256	32 x 32	64 x 64 x 96	64 x 64 x 96	32 x 32 x 32	64 x 64 x 96
# slices	30	32	96	96	32	96
Zero filling factor	0	2	2	2	2	2
# repetitions	1	1 per flip angle	1 per flip angle	15	6 per flip angle	5
Purpose of scan	Anatomic image for brain region segmentation	Estimation of pre-contrast T_1 and k	Estimation of pre-contrast T_1 and k	Estimation of SSS signals Estimation of K^{trans}	Estimation of PS_w	Estimation of K^{trans}

Figure 1

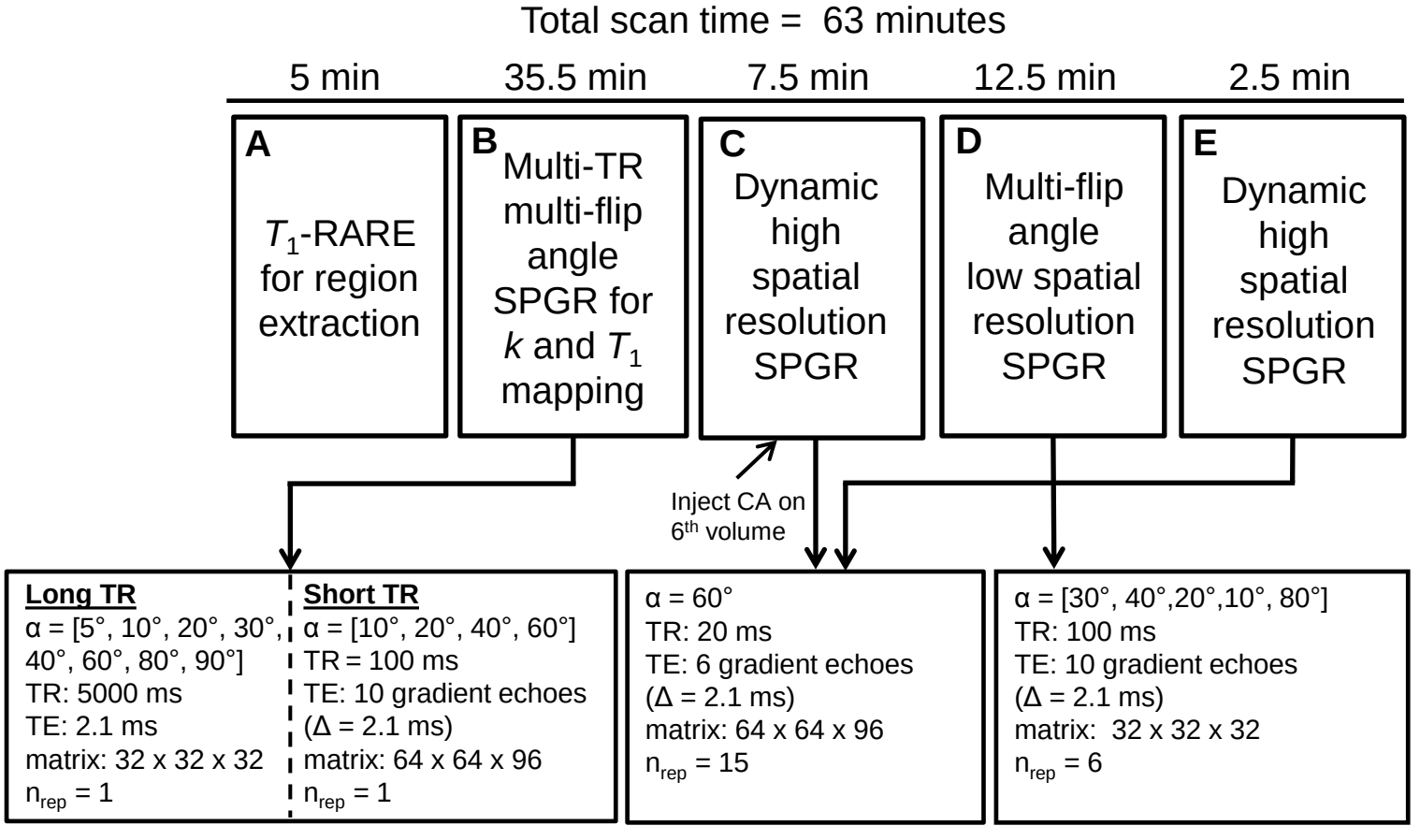
Total scan time = 63 minutes
5 min
35.5 min
7.5 min
12.5 min
2.5 min
A
T_1-RARE for region extraction
B
Multi-TR multi-flip angle SPGR for k and T_1 mapping
C
Dynamic high spatial resolution SPGR
D
Multi-flip angle low spatial resolution SPGR
E
Dynamic high spatial resolution SPGR
Inject CA on 6th volume
Long TR
α = [5°, 10°, 20°, 30°, 40°, 60°, 80°, 90°]
TR: 5000 ms
TE: 2.1 ms
matrix: 32 x 32 x 32
n_{rep} = 1
Short TR
α = [10°, 20°, 40°, 60°]
TR = 100 ms
TE: 10 gradient echoes
(Δ = 2.1 ms)
matrix: 64 x 64 x 96
n_{rep} = 1
α = 60°
TR: 20 ms
TE: 6 gradient echoes
(Δ = 2.1 ms)
matrix: 64 x 64 x 96
n_{rep} = 15
α = [30°, 40°,20°,10°, 80°]
TR: 100 ms
TE: 10 gradient echoes
(Δ = 2.1 ms)
matrix: 32 x 32 x 32
n_{rep} = 6

Figure 2

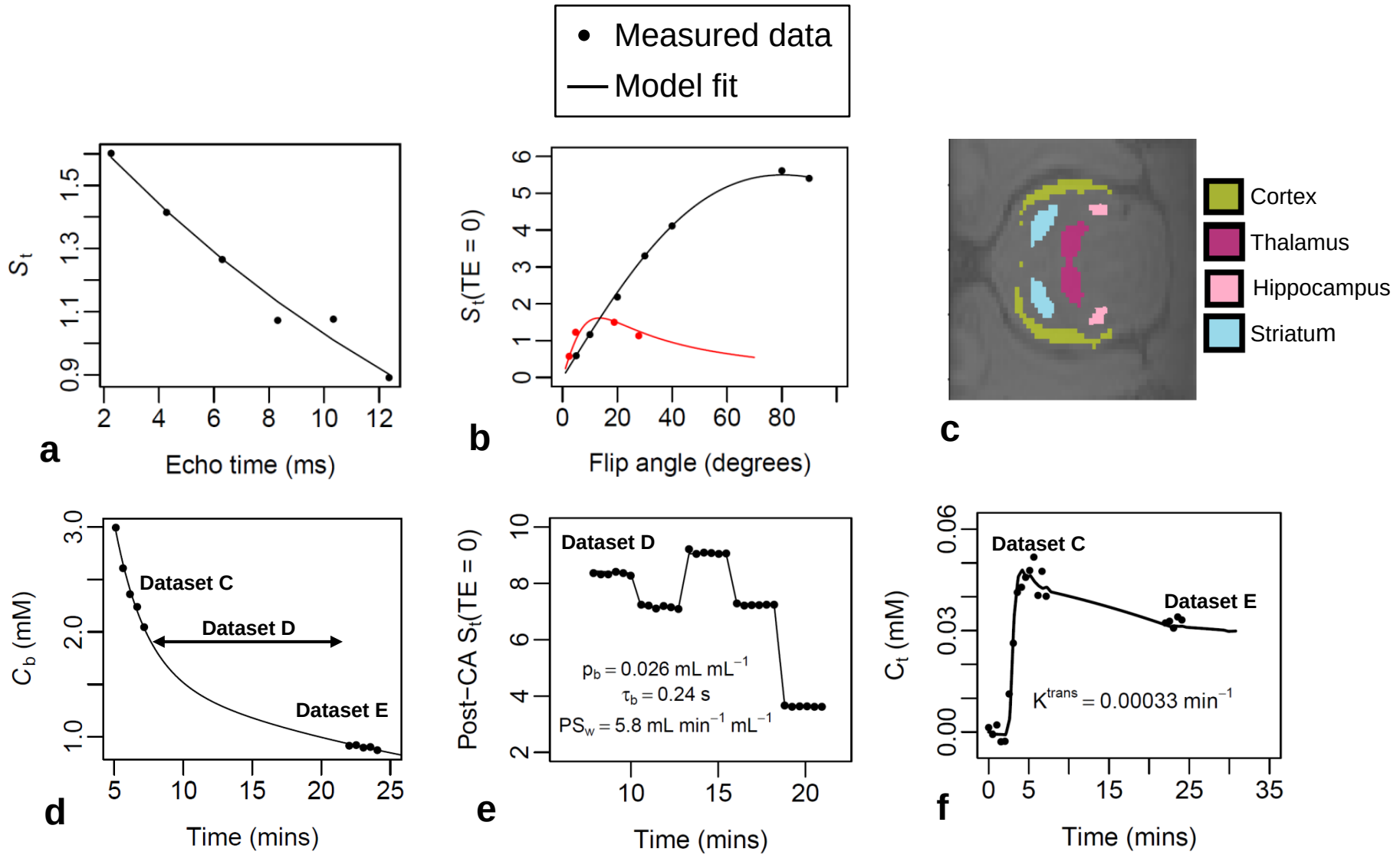
Measured data
Model fit
S_t
Echo time (ms)
a
$S_t(TE = 0)$
Flip angle (degrees)
b
Cortex
Thalamus
Hippocampus
Striatum
c
C_b (mM)
Dataset C
Dataset D
Dataset E
Time (mins)
d
Post−CA $S_t(TE = 0)$
Dataset D
$p_b = 0.026$ mL mL^{-1}
$\tau_b = 0.24$ s
$PS_w = 5.8$ mL min^{-1} mL^{-1}
Time (mins)
e
C_t (mM)
Dataset C
Dataset E
$K^{trans} = 0.00033$ min^{-1}
Time (mins)
f

Figure 3

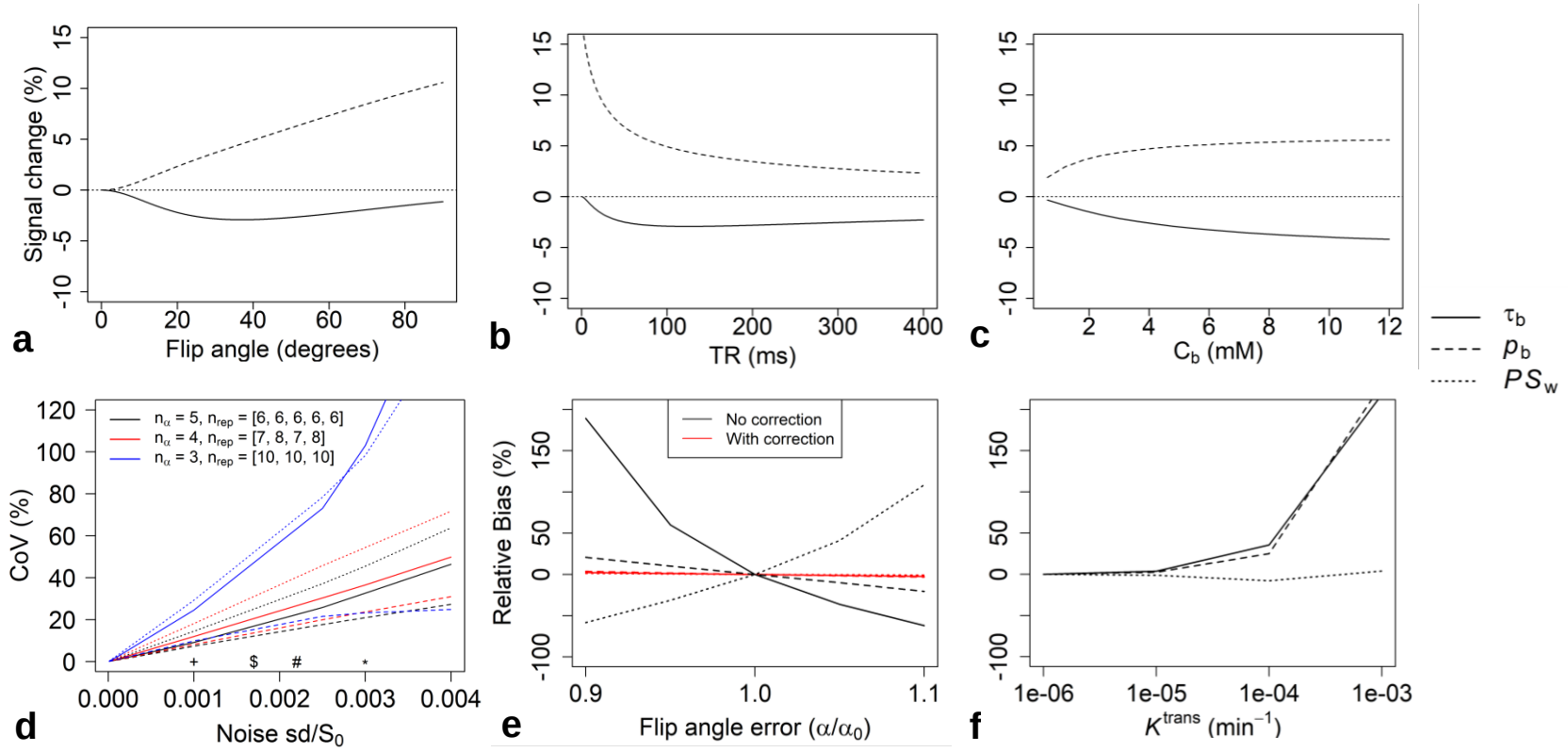
Signal change (%)
Flip angle (degrees)
a
TR (ms)
b
C_b (mM)
c
τ_b
p_b
PS_w
CoV (%)
n_α = 5, n_{rep} = [6, 6, 6, 6, 6]
n_α = 4, n_{rep} = [7, 8, 7, 8]
n_α = 3, n_{rep} = [10, 10, 10]
Noise sd/S_0
d
Relative Bias (%)
No correction
With correction
Flip angle error (α/α_0)
e
K^{trans} (min^{-1})
f

Figure 4

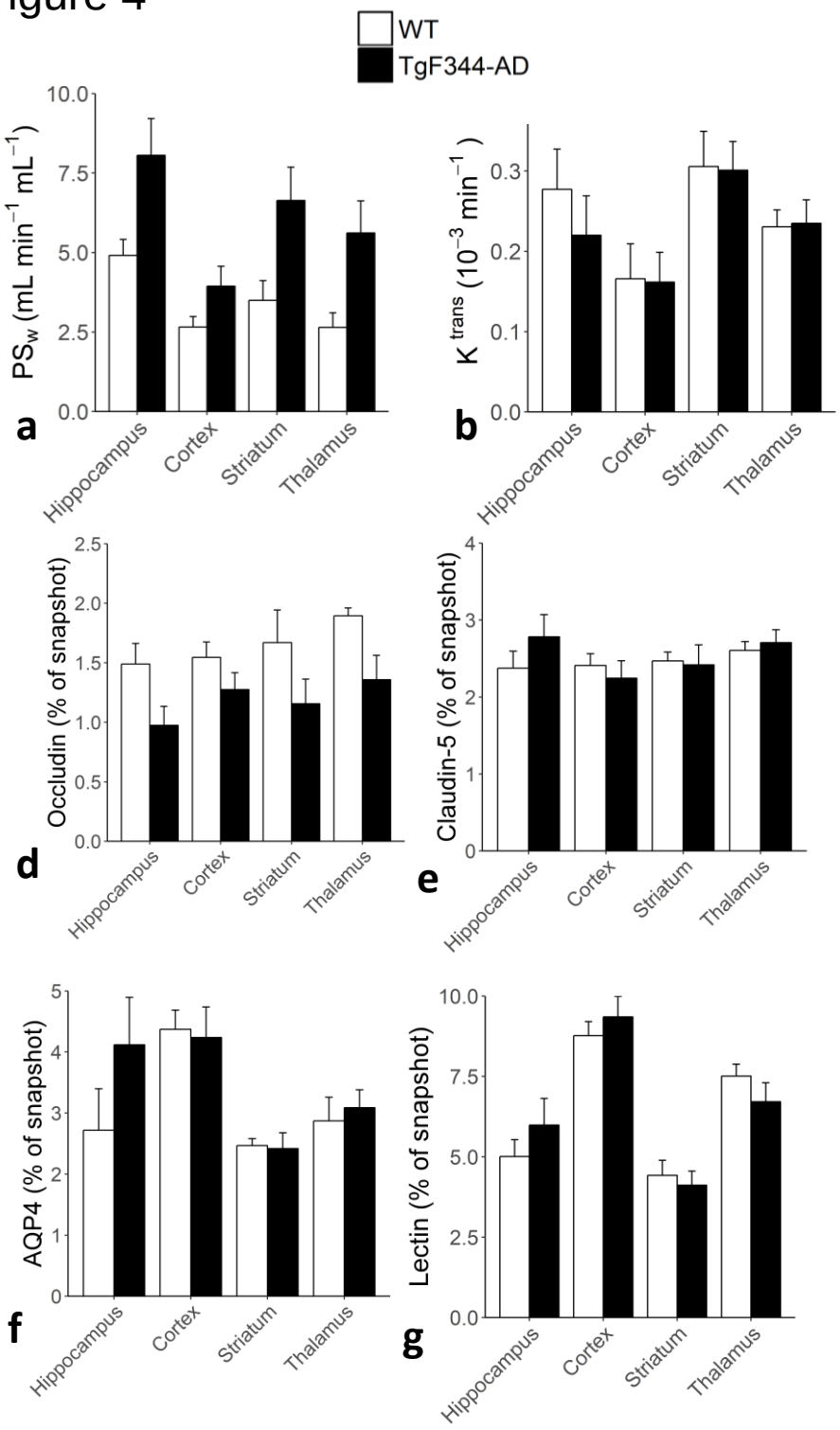
WT
TgF344-AD
PS_w (mL min^{-1} mL^{-1})
a
K^{trans} (10^{-3} min^{-1})
b
Occludin (% of snapshot)
d
Claudin-5 (% of snapshot)
e
AQP4 (% of snapshot)
f
Lectin (% of snapshot)
g
Hippocampus
Cortex
Striatum
Thalamus

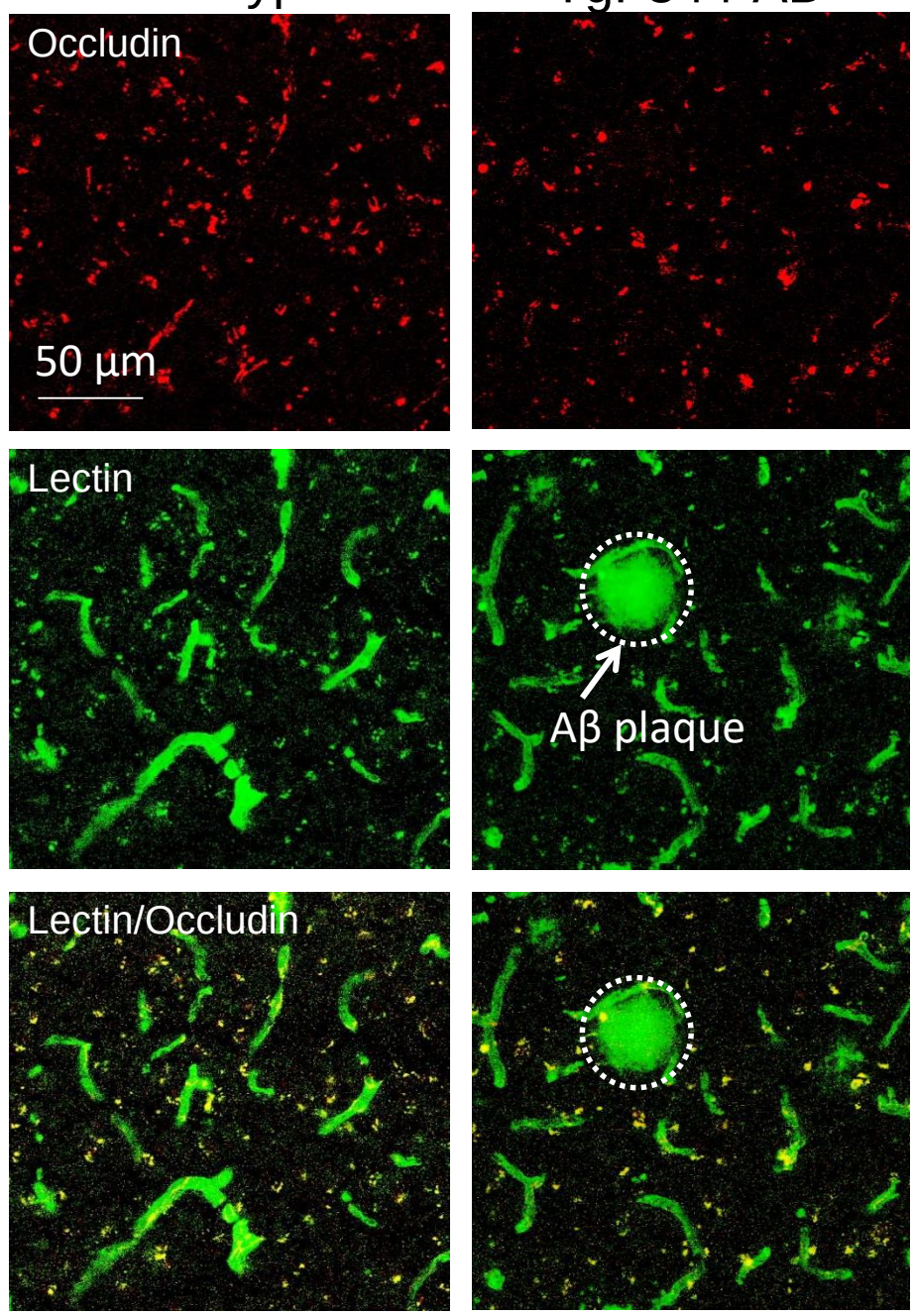
c
Wildtype
TgF344-AD
Occludin
50 µm
Lectin
Aβ plaque
Lectin/Occludin

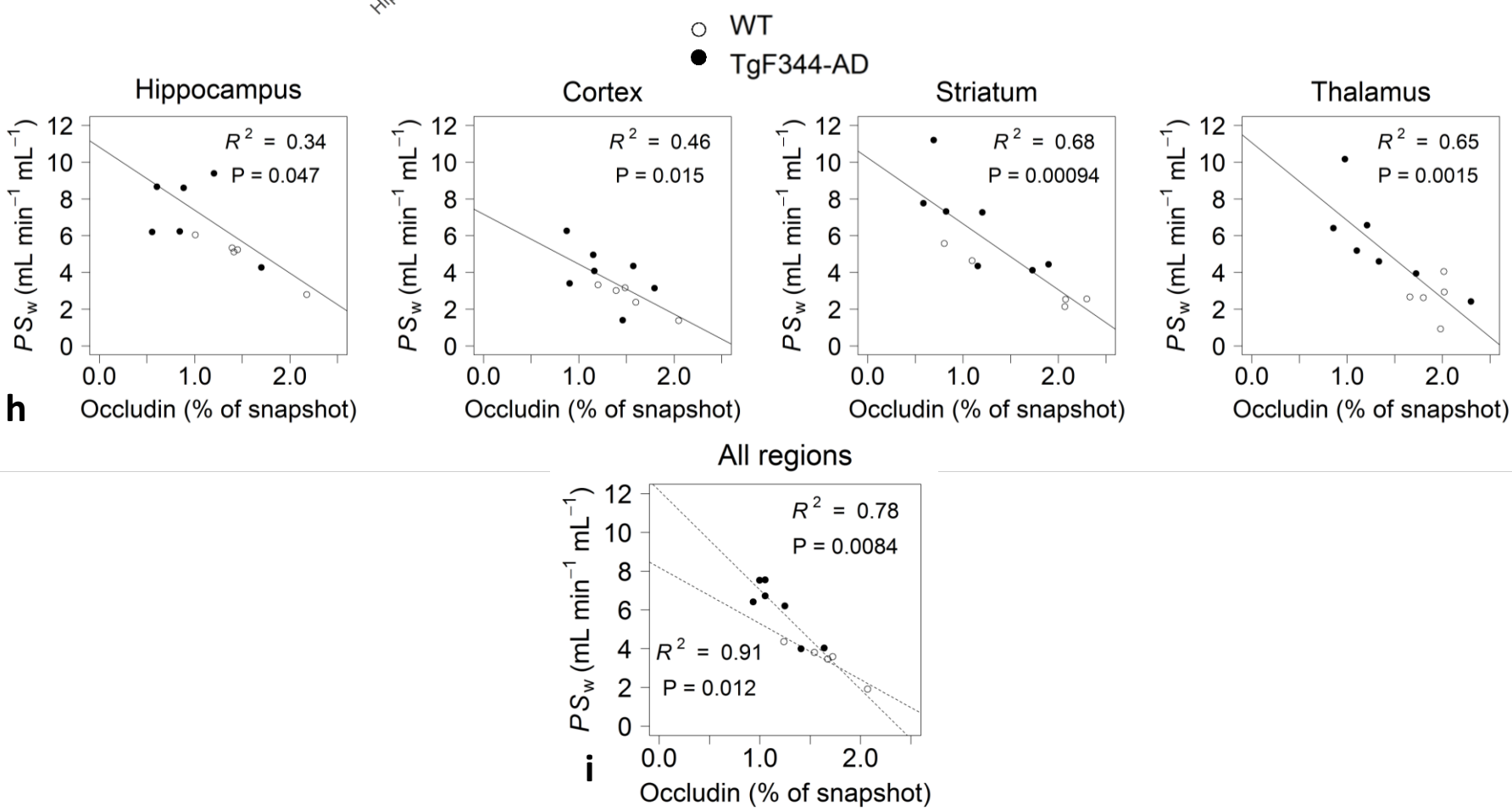
WT
TgF344-AD
Hippocampus
Cortex
Striatum
Thalamus
R^2 = 0.34
P = 0.047
R^2 = 0.46
P = 0.015
R^2 = 0.68
P = 0.00094
R^2 = 0.65
P = 0.0015
PS_w (mL min^{-1} mL^{-1})
Occludin (% of snapshot)
h
All regions
R^2 = 0.78
P = 0.0084
R^2 = 0.91
P = 0.012
i

Figure 5

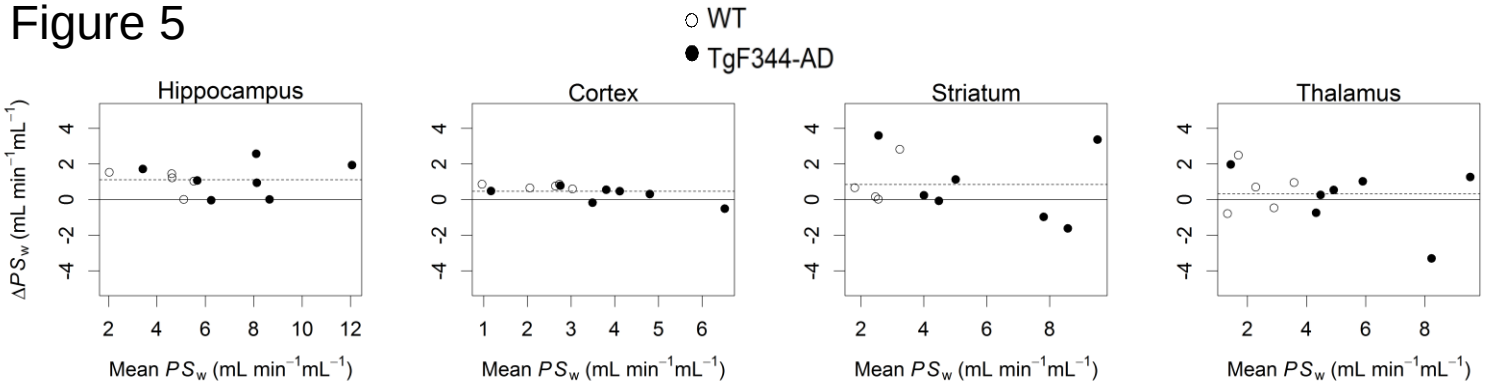
WT
TgF344-AD
Hippocampus
Cortex
Striatum
Thalamus
ΔPS_w (mL min⁻¹mL⁻¹)
Mean PS_w (mL min⁻¹mL⁻¹)